Fiber-optic combined FPI/FBG sensors for monitoring of radiofrequency thermal ablation of liver tumors: *ex vivo* experiments

Daniele Tosi,[1,*] Edoardo Gino Macchi,[2] Giovanni Braschi,[2] Alfredo Cigada,[3] Mario Gallati,[2] Sandro Rossi,[4] Sven Poeggel,[1] Gabriel Leen,[1] and Elfed Lewis[1]

[1]University of Limerick, Optical Fibre Sensors Research Centre, Limerick, Ireland

[2]Universita' di Pavia, Dipartimento di Ingegneria Civile ed Architettura, via Ferrata 3, 27100 Pavia (PV), Italy

[3]Politecnico di Milano, Dipartimento di Meccanica, via La Masa 34, 20158 Milano (MI), Italy

[4]IRCCS Policlinico San Matteo Foundation, VI Department of Internal Medicine, v.le Golgi 17, 27100 Pavia (PV), Italy

*Corresponding author: daniele.tosi@ul.ie

1. Introduction

Thermal ablation is a widespread therapy to treat tumors of 3–5 cm in size [1–3]. After diagnosing and locating the tumor through imaging (e.g., ultrasound, MRI, CAT scan), the radiofrequency ablation (RFA) procedure consists of selectively heating the tumor area by means of a localized energy source. Over 60°C cells death is instantaneous [4]; in addition, chemotherapy is prescribed afterward as an additional safety measure. The high selectivity, low invasiveness, and capability of dealing with both small and large tumors make thermal ablation a popular therapy. The three main procedures involving thermal ablation are RFA [5–8]; microwave ablation [9–11], in which heat is generated by Joule effect through an electromagnetic (EM) field; and laser ablation, where a laser is used [12]. RFA is the most common and less invasive procedure, and can usually be handled as an outpatient procedure.

In RFA, an EM field is generated within the patient by means of an active electrode (needle) positioned in contact with the tumor, with the tip as close as possible to its focal point, and a passive electrode placed on the patient's back. A radiofrequency (RF) generator, with 350–500 kHz emission frequency, creates an electric potential difference between the

electrodes and the current thereby generated induces a strong heating near the active electrode where the current density is very high. The surrounding tissue is heated by conduction; with a treatment of up to 40 min in duration, it is possible to treat small- and midsize tumors (up to 4 cm in size).

RFA is currently a standard procedure in cancer treatment, especially adopted for primary and secondary liver tumors; however, its application for large tumors is limited by liquid-vapor phase change. The main constituent of most biological tissues, including liver tissue, is water; over about 100°C the phase change takes place and, since vapor is a good dielectric, it progressively insulates the active electrode leading to the interruption of the ablation procedure [13,14]. The vaporization of the liquids contained in the tissue also generates a pressure increase in the heating point; this is particularly significant for encapsulated tumors since it might cause the dislodgement and scattering of malignant cells around the ablated tumor [15–17].

The research carried out by the authors, in connection with San Matteo Hospital in Pavia, Italy, is focused on improving the understanding of the physical phenomena connected with RFA in the liver, in order to develop a sound heating model based on the physical phenomena occurring during RFA, and on enhancing the current RFA technology to improve efficiency and invasiveness. A key asset is the possibility to perform a monitoring of both pressure and temperature in contact of the ablation point. This allows driving the RFA model with the physical data, improving the understanding of the phenomena connected with the interruption of the RFA procedure; furthermore, it can lead to a better control of RFA efficiency.

In this medical application, the technical requirements related to sensing are challenging: (1) the sensing probe has to measure both pressure and temperature in a very localized region; (2) the sensor must be minimally invasive, miniature size, and biocompatible; (3) immunity to electromagnetic interference (EMI) is necessary due to the close proximity of the sensor to the active; (4) the extremely steep gradients of both temperature and pressure require that the sensor has very low cross sensitivity between these two parameters. Unlike standard microelectromechanical systems (MEMS), optical fiber sensors [18] are a suitable candidate, due to their miniature size (e.g., 0.2 mm diameter), tensile and compressive strength (which allows safe insertion despite the small size), immunity to EMI, and the ability to measure multiple parameters while maintaining a small overall size.

The most popular approach for development of medical pressure sensors based on optical fibers is extrinsic Fabry–Perot interferometry (EFPI) [19,20]. Several EFPI-based configurations have been recently presented [21–28]; in addition, EFPI-based medical devices are commercially available [29]. It is possible to combine an EFPI probe with a fiber Bragg grating (FBG) [30,31], acting as temperature sensor in proximity of the EFPI sensor, to provide a dual sensing with cross compensation; such configuration has been proposed in [26–28]. In [26,27], a dual EFPI/FBG sensor is proposed, achieving 1.68 nm/kPa pressure sensitivity, and 1.7 nm/°C cross sensitivity; [28] proposes a novel manufacturing technique based on UV mold, with limited biocompatibility, and 1.53 nm/kPa and 15.8 nm/°C sensitivity coefficients. Commercial devices [29], on the other side, do not offer dual sensing option, and are not compatible with >60°C temperature operation.

Depending on duration, RF power and clinical situation, during RFA the temperature rises over 100°C and the relative pressure may rise over 50 kPa at the ablation point; gradients are extremely steep as no pressure and no temperature rise can be observed even only a few centimeters far from ablation point. The current state of the art of dual EFPI/FBG [26–28] does not allow an adequate cross compensation, as the temperature-sensing FBG is located few millimeters far from the EFPI tip, hence is exposed to a much different temperature making the compensation ineffective. In this paper, we present a combined EFPI/FBG probe in which the EFPI sensor exhibits a small temperature coefficient (51.9 pm/°C, 32 times smaller than [26] and 304 times smaller than [28]); this allows a neat separation between temperature and pressure sensing, which is essential in presence of such a steep gradient. The dual probe exhibits accuracy of 40 Pa and 0.2°C and is based on an all-glass design, which complies with basic biocompatibility requirements. Using the proposed probe, we provide results of pressure and temperature measurements during uniform RF heating in a test chamber, and during an *ex vivo* RF ablation of porcine liver samples using a tip electrode.

The paper is arranged as follows: Section 2 describes the fabrication of the EFPI/FBG sensing probe; Section 3 describes the sensor calibration and compensation of thermal effects; Section 4 reports simultaneous pressure and temperature measurement in a RF-heated test chamber; Section 5 shows results from two *ex vivo* RFA experiments in porcine liver; finally, in Section 6 we draw conclusions.

2. Sensor Fabrication

The fabrication of dual EFPI/FBG sensor is based on three sequential steps, as shown in Fig. 1: inscription of the FBG, fabrication of the Fabry–Perot cavity through splicing, and etching of the diaphragm tip. All components included in the setup, including optical fibers, operate in the third optical window around 1550 nm.

In first place, a uniform FBG is inscribed on a single-mode fiber (SM 10/125 μm, outer buffer 150 μm) using a phase mask technique [32]: the fiber is stripped and exposed to UV light through a phase
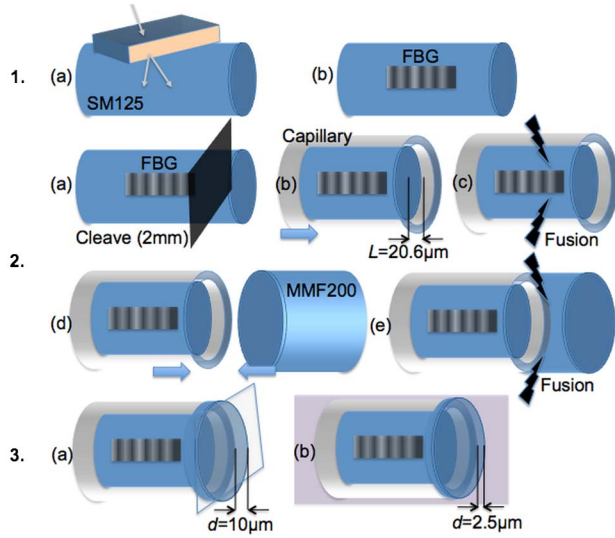
Fig. 1. Fabrication process of the EFPI/FBG probe. (1) Fabrication of the FBG: (a) by exposing a single-mode SM125 fiber to UV light through a phase mask, we obtain a 4-mm long uniform FBG (b). (2) Formation of the sensing cavity: (a) the SM fiber is cleaved about 2 mm far from the FBG end, and (b) by means of micropositioners is slid into a hollow capillary until a gap length $L = 20.6$ μm is obtained. (c) Then, a splice is made to fuse SM fiber and capillary. The obtained cavity is (d) aligned to a multimode MMF200 fiber, having same diameter of the capillary, using micropositioners; when the best alignment is found, (e) a second splice is performed to enclose the air-gap in-between the fibers and the capillary. All fibers are polished prior to alignment and splicing. (3) Diaphragm shortening: (a) the MMF diaphragm is cleaved and manually polished until a length of 10 μm is obtained; then, (b) the probe is immersed in a HF bath to accurately etch the diaphragm until reaching 2.5 μm thickness.

mask. The resulting FBG has reflectivity 95% at 1551.50 nm pitch wavelength (room temperature), and nominal thermal coefficient of the FBG is 10.6 pm/°C. The grating length has been selected as 4 mm, resulting as a trade-off between short active region and good reflectivity after the following splicing operations.
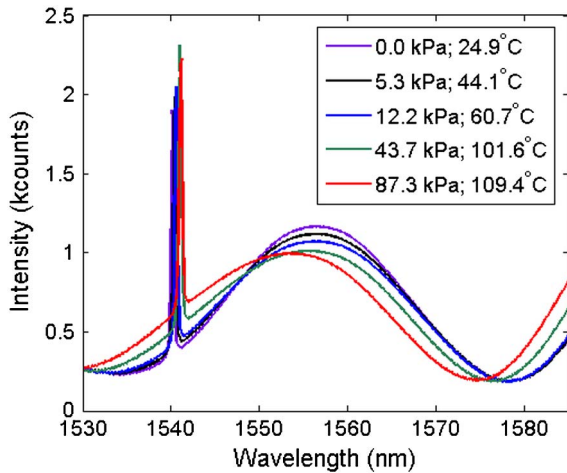

Fig. 2. Combined EFPI/FBG spectrum for different values of pressure and temperature.

After FBG photoinscription, the EFPI cavity is fabricated in proximity of the FBG. The SM fiber is cleaved 2 mm far from the FBG tail with a precision cleaver, which represents the shortest distance, considering the splicing machine, between the EFPI and FBG active regions without deteriorating the sensing quality. Then, the SM fiber is inserted in a glass capillary, having 130/200 μm inner/outer diameter, by means of dual-stage 3D micropositioners. Prior to insertion, the capillary is $\lambda/5$-polished. A gap is formed between the SM and capillary end, which represents the Fabry–Perot sensing cavity, with a thickness $L = 20.6$ μm. After achieving the correct positioning, the SM fiber is fused to the capillary using a splicer in full manual mode. The fusion point is located in proximity of the FBG; as a consequence, the splice operation [2(c) in Fig. 1] results in a small detuning of the FBG pitch wavelength (1550.45 nm) and of the thermo-optic coefficient (10.7 pm/°C) and a conspicuous reduction of the reflectivity (from initial 95%–9%), as in [27]. A standard multimode fiber (MM 62.5/200 μm) is then applied to the tip, serving as diaphragm. The fiber is first cleaved, then manually $\lambda/5$-polished. A second splice is performed fusing the MM fiber to the capillary, previously fused to the SM fiber. No significant change of the air-gap L occurs during the capillary-to-MM splice.

This approach allows building an air-gap in between the SM and the MM fiber. The structure hereby formed is all-glass, achieving a perfect biocompatibility without requiring additional encapsulation as in [29] or epoxy or bonds as in [28]. The splicing quality [2(c) and 2(e) in Fig. 1] ensures an excellent sealing of the glass structure: this leads to a small thermal coefficient, and remarkable stability even in long operations. The mechanical strength of the glass diaphragm is sufficient to sustain the insertion and pressure application in the liver tissue, as opposed to flexible diaphragms [23] that are excessively fragile for insertion.

Finally, the sensor is functionalized to pressure sensing by etching the diaphragm to a thickness $d \sim 2.5$ μm; the pressure sensitivity is proportional to d^{-3} [26]. Manual polishing is first applied, using 1/3 μm polishing paper, reducing the thickness of the diaphragm to 10 μm. Subsequently, the diaphragm is wet-etched in hydrofluoric acid (HF), using an online monitoring technique as in [33]. HF-etching allows reaching 2.5-μm thickness, which is a trade-off between pressure sensitivity and mechanical resistance; this allows achieving a sensitivity of 1.6 nm/kPa. After etching, residual HF is evacuated from the tip by heating the probe at 200°C in an oven for 10 min, allowing HF to completely evaporate from any interstice.

Using this technique, several sensors have been fabricated, achieving sensitivity 1.0–1.6 nm/kPa and having air-gap length 20–22 μm. The probes have maximum thickness of 0.2 mm on the tip. All data reported hereafter are related to a sample probe

having the aforementioned 1.6 nm/kPa pressure sensitivity, 20.6 µm air-gap length, and 10.7 pm/°C FBG thermo-optic coefficient.

3. Pressure and Temperature Calibration

The interrogation setup, used for fabrication, calibration and experimental measurements, is based on a spectrometric approach [34]. The setup consists of a broadband source (Opto-Link ASE C+L-Band) with 20 mW emission power, coupled to the EFPI/FBG probe through a 3 dB coupler. The backreflection is collected with a spectrometer (Ibsen I-MON) operating on the 1520–1600 nm bandwidth. The spectrometer has 512 pixel on the wavelength axis, corresponding to 156 pm resolution grid.

Figure 2 shows the reflection spectrum of the sensing probe, recorded with the spectrometer; the spectrum is normalized in order to remove the contribution of the broadband source and integrated over 36 ms. Spectra are reported for growing temperature and pressure, exerted in a pressure and temperature joint chamber. At zero pressure, the EFPI has a maximum reflectivity close to the nominal value of 4% due to glass/air interface; on the other hand, the FBG peak reflectivity is 9%. The chart shows the different spectral profile of the EFPI and FBG, whereas the former has a broad envelope (>30 nm) and the latter has a narrow bandwidth; hence, the two contributions are treated separately. The peak wavelength of the FBG is estimated using an oversampling and correlation technique, as presented in [35]: a polyphase filtering, with upsampling factor 127, is applied on the FBG spectral slice with 4 nm width, and the wavelength shift is estimated by computing the mutual correlation between measured and reference spectrum. This way, it is possible to achieve peak wavelength shift ($\Delta\lambda$) tracking with 2 pm resolution. The estimation of the Fabry–Perot cavity length is performed using a normalized quadrature-point detection as described in [27], where the 1567.5 nm Q-point is tracked; this allows estimating the air-gap compression ΔL relative to the initial length L.

This way, it is possible to obtain the calibration curves as in Fig. 3, whereas EFPI and FBG have been individually calibrated for pressure and temperature, respectively. Pressure calibration has been performed in a pressure chamber, at constant temperature. Temperature calibration has been performed in a climatic chamber by applying temperature ramps at constant humidity. Figure 3(a) shows the EFPI experimental calibration curve obtained in a pressure chamber, reporting the air-gap cavity compression ΔL as a function of applied pressure on the 0–70 kPa range. The chart shows an excellent linearity on the whole range, with a sensitivity $s_P = 1.60$ nm/kPa. Figure 3(b) shows the FBG temperature calibration, showing as well an excellent linearity, on the range 27°C–90°C. The slope is estimated as $k_T = 10.70$ pm/°C. Specific low-pressure detection, in a burette, allow estimate the pressure
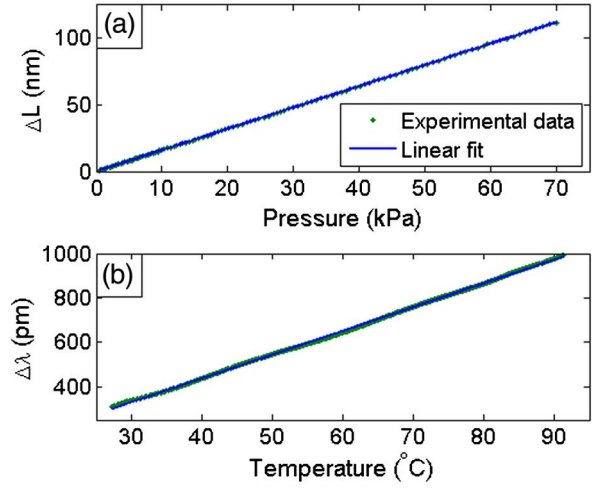

Fig. 3. Pressure and temperature sensitivity of the EFPI/FBG probe. (a) Pressure sensitivity, evaluated as air-gap compression ΔL as a function of applied pressure; slope = 1.60 nm/kPa. (b) Temperature sensitivity of the FBG probe, evaluated as peak wavelength shift $\Delta\lambda$ as a function of temperature variation; slope = 10.70 pm/°C.

accuracy as 0.3 mmHg (40 Pa); temperature accuracy is 0.2°C, and it is dominated by the 2 pm wavelength detection resolution.

In this specific application, the cross sensitivity plays a fundamental role: because of the different spatial positioning of the FBG and EFPI sensing area, in the presence of steep thermal and pressure gradients (often higher than 40°C/cm and 30 kPa/cm) during the RFA operation, the compensation of thermal effects cannot be perfectly accomplished, since EFPI and FBG are exposed to different temperatures. Pressure sensitivity of the FBG (nominal: $2 \cdot 10^{-6}$ MPa^{-1} [28]) is negligible and is approximated to zero, while temperature sensitivity of the EFPI is the dominant term. Figure 4 shows the temperature sensitivity of the EFPI, reporting the air-gap compression as a function of applied temperature; the sensor is
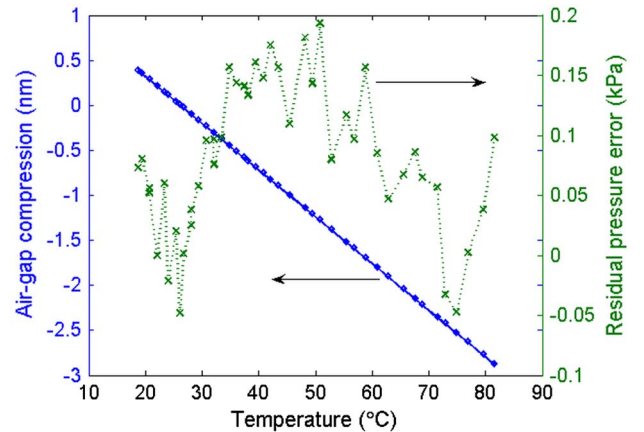

Fig. 4. Temperature sensitivity of the EFPI probe. The chart reports the air-gap compression as a function of temperature (left axis), with an estimated slope 51.9 pm/°C, and residual error after temperature compensation (right axis).

initialized at ambient temperature 25°C. The temperature dependence is almost perfectly linear, and the estimated slope is $s_T = -0.0519$ nm/°C. This thermal dependence is extremely low, compared to the 1.60 nm/kPa pressure sensitivity, and corresponds to -0.032 kPa/°C detuning coefficient for noncompensated temperature. Compared to previous literature, the thermal sensitivity of the EFPI hereby obtained is 32.7 times smaller than [26] (1.7 nm/°C) and 304.4 times smaller than [28] (15.8 nm/°C).

The thermal compensation, as in [26–28], can be performed by including all sensitivity terms, and jointly estimating pressure ΔP and temperature variation ΔT from the measured air-gap compression ΔL and FBG peak wavelength shift $\Delta \lambda$:

$$\begin{bmatrix} \Delta L \\ \Delta \lambda \end{bmatrix} = \begin{bmatrix} s_P & s_T \\ 0 & k_T \end{bmatrix} \begin{bmatrix} \Delta P \\ \Delta T \end{bmatrix}$$
$$= \begin{bmatrix} 1.60 \text{ nm/kPa} & -0.0519 \text{ nm/°C} \\ 0 & 10.70 \text{ pm/°C} \end{bmatrix} \begin{bmatrix} \Delta P \\ \Delta T \end{bmatrix} \tag{1}$$

and by reversing the inner matrix,

$$\begin{bmatrix} \Delta P \\ \Delta T \end{bmatrix} = \begin{bmatrix} 0.625 \text{ kP}a\text{/nm} & 3.03 \cdot 10^{-3} \text{°C/pm} \\ 0 & 0.09346 \text{°C/pm} \end{bmatrix} \begin{bmatrix} \Delta L \\ \Delta \lambda \end{bmatrix}, \tag{2}$$

it is possible to achieve the cross-compensation matrix. Figure 4 reports, for each 18°C–82°C temperature, the residual pressure error after compensation, which ranges from -0.05 to 0.20 kPa.

If we assume a conservative thermal gradient of 40°C/cm, and a 0.4 cm mismatch between the FBG center and Fabry–Perot cavity, the resulting 16°C mismatch between the two sensors would induce a 0.52 kPa pressure error, which is reasonably acceptable. On the other hand, [26] would introduce a 17 kPa error, and [28] a 158 kPa error due to the thermal detuning, which would not be tolerable. Hence, the sensor fabrication technique shown in this paper demonstrates an extremely low thermal cross sensitivity, which is essential to address RFA monitoring.

4. RF Heating in Test Chamber

In the next section, the EFPI/FBG probe has been used to monitor *ex vivo* RFA, where no reference sensor is available. Hence, a RF heating test has been carried out on both saline and liver tissue in an *ad hoc* test chamber, which hosts both the fiber-optic and reference MEMS sensors, to validate the correct operation. The measurement setup is shown in Fig. 5. The test environment is a cylindrical chamber with electrically conductive bases equipped with an internal piston (with negligible friction) that separates two volumes. One volume is filled with the tested medium (saline or liver tissue) and the other is occupied by air. The chamber has four variable airtight inlets. A RF generator, with 480 kHz emission frequency, heats up the test medium in a uniform
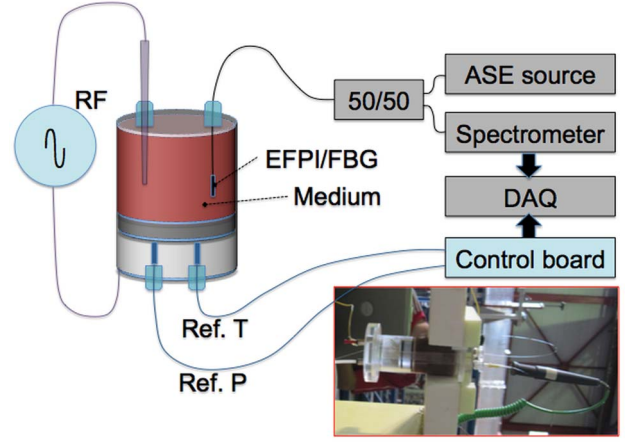

Fig. 5. RF-heated test chamber setup. The inset shows a picture of the setup, loaded with liver on the top chamber.

way; the EFPI/FBG probe is placed in the test medium through the inlet, protecting the insertion with a plastic tube removed afterward. A reference MEMS sensor (Epcos B57861 NTC thermistor) is used to measure the medium temperature. Upon heating, the medium is expanded and pushes the piston, increasing the air pressure. At equilibrium both medium and air pressure must be equal; the reference pressure is therefore measured in air by means of a piezoresistive sensor (Honeywell 26PCDFA6G, accuracy 0.1 kPa, compensated up to 50°C). The fiber-optic setup is completed by a broadband ASE source, a 50/50 coupler, and a spectrometer. MEMS sensors are connected by a custom control board; data acquisition is jointly handled for both fiber-optic and MEMS sensors, with separate software programs. The system is initialized when RF heating is started. The RF generator (suitable for medical use) works in the impedance range 20–300 Ω, and embeds an impedance-meter, that releases the RF power when the impedance falls below threshold. The electrical signal provided by the RF generator is monitored with an oscilloscope in a closed feedback loop.

In the first test, the chamber is loaded with a 0.2% NaCl saline solution; the measurement result is shown in Fig. 6. From the initial start, the temperature rises with an approximately linear slope reaching a peak temperature of 119°C (580 s). Then, the power supply is manually stopped, triggering the cooling stage: the temperature decreases with a much slower rate, reaching 91°C at the end of the test (1300 s). The pressure chart shows a slow increase up to 420 s, reaching 17 kPa; then, a 8 kPa pressure drop is observed. At this point, the pressure rapidly increases, up to 96 kPa at the 580 s peak point. When the RF generator releases the circuit, the pressure drops to 30 kPa approximately 200 s after the peak, and terminates the test at 4 kPa. The chart shows a good qualitative match between the EFPI/FBG and the reference MEMS probes. Aside from a slight initial misalignment, the
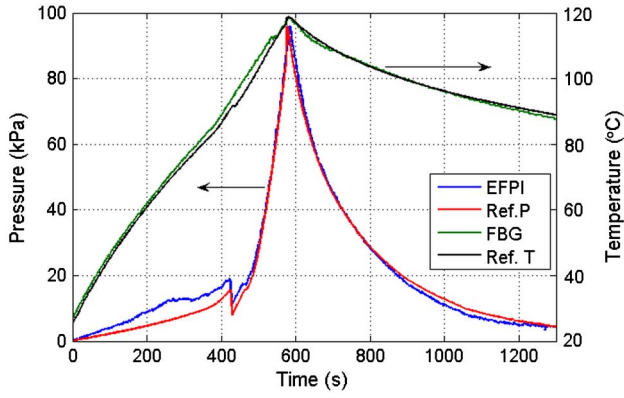
Fig. 6. Pressure and temperature readout for simulated RFA, with test chamber loaded with saline solution (0.2% NaCl). The chart reports pressure (left) and temperature (right) measurements, acquired in real time.
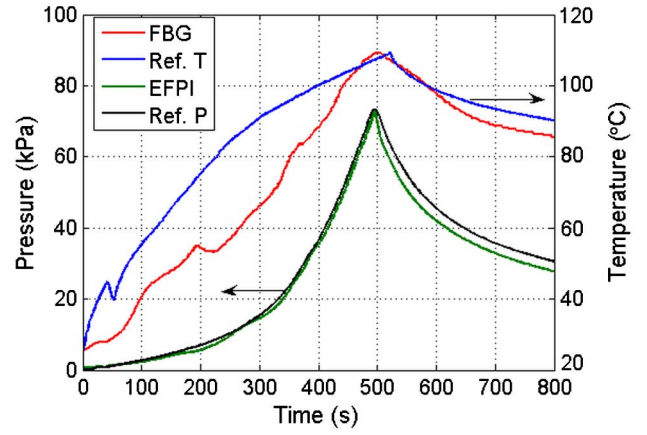

Fig. 7. Pressure and temperature readouts for RF heating of porcine liver tissue. The chart reports pressure (left) and temperature (right) measurements, acquired in real time.

temperature rise observed with the FBG is slightly higher than the reference, particularly for the high-temperature part of the curve; on the other hand, the temperature recorded with the FBG appears to decrease slightly faster after the peak. Such difference can be attributed to the fact that the sensors are placed inside the medium in different positions, and partially to the slower slew rate of the MEMS versus the instantaneous response of the FBG. The pressure chart shows a good match on the rising and decreasing parts, with a slight misalignment on the peak position. In the initial part of the chart, the EFPI sensor trace rises more than the reference MEMS; such behavior may be attributed to slightly different pressure values between top and bottom chambers (due to limiting friction). Furthermore, the pressure trace measured by the EFPI appears to have a slight and nonconstant delay over the whole measurement cycle: this can be attributable to the thermal behavior of the reference sensor, which is temperature-compensated up to 50°C and appears to introduce a thermal-dependant error over this threshold.

A second test has been performed loading the chamber with porcine liver, as shown in Fig. 5 (inset). The top chamber is loaded with liver; the EFPI/FBG fiber-optic probe is guided into the liver through an airtight inlet by means of a protective catheter, removed after insertion, and a red laser is used for illuminating the fiber tip. The temperature and pressure reference sensors are positioned, respectively, in the liver tissue and in the bottom chamber, which is filled with air. The initial impedance of the liver is ~90 Ω; the RF generator is turned on at the measurement start, and is automatically disconnected after 498 s, when the impedance exceeds the operating range of the RF generator. The experimental measurement is reported in Fig. 7. The pressure chart shows a good quantitative agreement between reference and EFPI probe, particularly during heating. Compared to Fig. 6, the pressure curve rises with a smaller slope, achieving a maximum value of

73 kPa. The EFPI readout appears to decrease faster than the reference MEMS. On the other hand, the temperature measurements appear to have only a qualitative match, with the temperature rising from ambient to 109°C and then slowly decreasing; however, the two traces appear to have a different trend, with the FBG having a smaller temperature increase. We attribute this mismatch to a nonuniform heating of the medium, whereas the MEMS sensor is positioned closer to the electrode and several air bubbles appear during the heating process. The 4-mm long FBG probe may be partially or entirely positioned in an area occupied by an air bubble, and since the air bubble is heated by heat conduction from the surrounding tissue the overall heating rate appears lower than the one measured by the MEMS.

The peculiarity of liver tissue and the abrupt joint variations of both temperature and pressure during RFA pose severe technological challenges for sensing technologies; the test in a RF-heated chamber hence is a good indicator on the possibility of using the dual EFPI/FBG probe in RFA, and demonstrates the low cross correlation between pressure and temperature.

5. *Ex vivo* RFA in Porcine Liver

Three experiments have been carried out in order to demonstrate proximal temperature and pressure detection in liver tissue. Tests have been performed *ex vivo* on porcine liver tissue, the natural phantom of human liver and generally used in RFA studies. Figure 8 shows the experimental setup for the first two measurements. The active electrode used for these RFA tests is a needle with 3 mm diameter and 10 mm active length, which is connected to the RF generator; the electrode penetrates the porcine liver for approximately 2 cm. The liver is placed on a metal plate that also acts as a passive electrode.

We anticipate that pressure traces will appear more noisy than in Figs. 6 and 7: this might be due to the greater heterogeneity of *ex vivo* native liver tissue that affects the change of refractive index of the liver through the ablation, and the change of
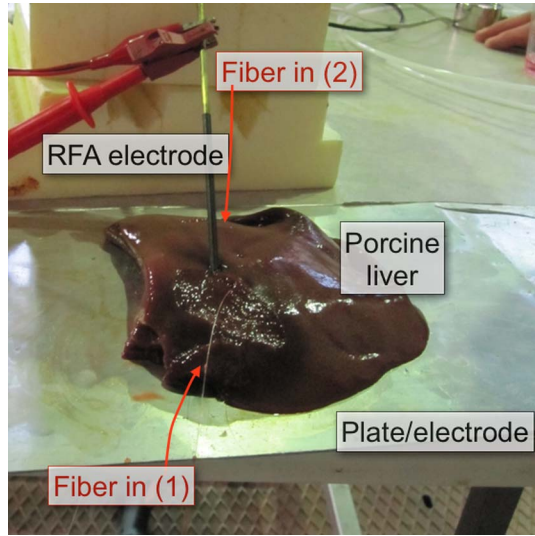
Fig. 8. Setup for *ex vivo* RFA demonstration. The active electrode is a hollow 3-mm needle inserted through the porcine liver tissue that is placed on a metal plate (acting as passive electrode). In the first experiment, the fiber has been guided in with a plastic catheter, which has subsequently been removed to leave the fiber in place; the second experiment has been performed with the fiber probe inserted through the hollow RFA needle.

Fig. 9. First RFA experiment: temperature and pressure traces.

relative position of the EFPI tip in front of the tissue. The liver acts as an external mirror, in which reflectance and phase change during the ablation due to liver expansion, pressure release, and externally induced vibrations. This can be compensated by means of thin (∼20 nm) deposition of biocompatible metal (Au or Ti) on the fiber tip, to decouple the EFPI spectrum from the external target by means of a high-reflectivity layer. This task, however, exceeds the experimental research hereby presented; in order to partially mitigate noise, we introduce a low-pass digital filter on the pressure trace (Butterworth 7th order, normalized cut-off frequency 0.04) and compensate for the delay introduced.

In the first experiment, the EFPI/FBG probe is guided in proximity of the ablation point. The insertion has been performed by means of a rigid catheter that allows penetrating the liver surface while protecting the fiber tip. A red laser has been used to position the EFPI tip approximately 0.8 cm far from the electrode needle tip. A picture of the experimental setup is shown in Fig. 8. A thermal ablation has been performed for approximately 4′45″ on the porcine liver, before the RF generator is self-disconnected. Pressure and temperature traces through RFA are shown in Fig. 9. We notice a small temperature and pressure increase in the measurement point: the temperature rises from 24.9°C to 30.7°C while the pressure rises from the initial zero to 6.2 kPa. In this RFA, we observe that the temperature rises initial with a linear slope, while the pressure has an initial 2.4 kPa steep growth. At the end of the RFA, the temperature rises with a steeper slope, and we observe a second pressure step of 3.5 kPa. The measurement shows that about
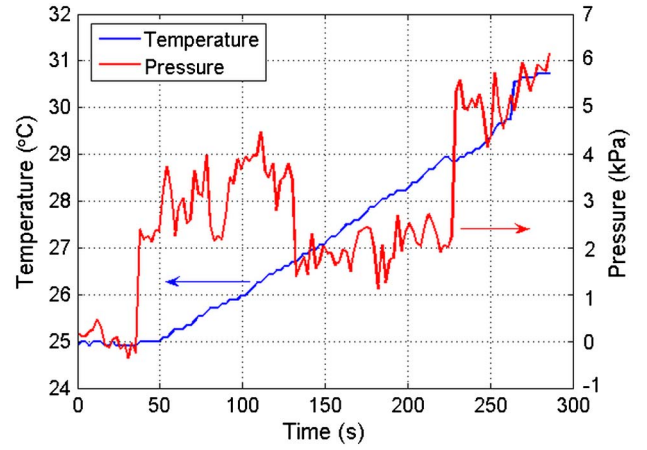
0.8 cm aside from needle tip, the pressure and temperature variations are limited. This shows that, as expected, the temperature and pressure gradients are very steep, in particular when small diameter active electrode and high powers are used.

In the second experiment, the EFPI/FBG probe is guided inside the hollow needle serving as the electrode. The fiber is initially retracted, then gently pushed against the liver; we estimate that the distance between fiber tip and needle is less than 1 mm. Porcine liver has been laid on a metallic plate, serving as a passive electrode, while the ablating electrode is inserted through the liver, about 1 cm above the plate. The experimental results of the RFA (5'30" duration) are reported in Fig. 10. From the initial ambient temperature, we observe an initial gradual rise, with the temperature achieving 80°C after 270 s. Then, the temperature rapidly grows with a quadratic slope, and achieves a 164° C peak after 330 s. As usual during the ablation, we initially observe gradual decrease of the impedance up to about a half of its starting value then, over 100°C, the impedance rises rapidly, exceeding the RF generator threshold at 330 s and therefore forcing the generator to shut down, having the temperature to fall back to ambient temperature in approximately 5 s. After an initial pressure decrease (-13 kPa), the
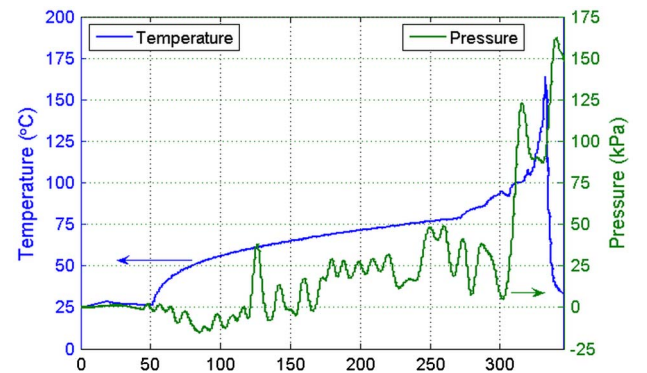

Fig. 10. Second RFA experiment: temperature and pressure traces; *x* axis shows time, in s.

pressure appears to have a slow rise until 300 s, achieving a maximum value close to 50 kPa. At 300 s we observe a steep pressure rise up to 124 kPa, followed by a pressure decrease to 87 kPa. When the RF generator shuts down, we observe a second pressure rise achieving a peak value of 162 kPa before declining. We observe a delay between temperature and pressure peaks, with the pressure peak having a 5 s delay with respect to temperature maximum. The observation of such peak values of temperature and pressure has an impact on the RFA analysis. The local peak temperature well exceeds the boiling point of water (main constituent of liver tissue), and the typical temperature values measured with (bigger) standard MEMS sensors during RFA (100°C–110°C). In addition, a pressure of over 100 kPa is an extremely high value that alters the heat transfer dynamics during the RF ablation.

A third experiment has been carried out and reported in Fig. 11. As shown in Fig. 12, in this experiment the fiber tip is located approximately 0.5 cm aside the needle tip. The ablation process has a total duration of 10'30". In this experiment we observe a less-than-linear gradual heating up to a maximum of 46°C. Then, as usual, the temperature drops after the RF generator is stopped (630 s). In correspondence of the temperature rise, we observe a slow pressure rise up to 7.5 kPa at 400 s; then, we observe a progressive rise up to 22 kPa when the RF generator shuts down. As in Fig. 10, we still observe a pressure rise (33 kPa maximum) after the RF generator stops. The effect of RFA is shown in Fig. 12: the elliptical profile of the ablated volume appears as a brighter color visible on the liver tissue, showing the outer profile. The heat is supplied near the active electrode tip, which is 0.6 cm far from the center of the elliptical trace. The EFPI/FBG probe is illuminated with a red light, showing the location of the tip in close proximity of the center of the ablation lesion; the picture shows a 0.5 cm misalignment between the fiber and active electrode tips.

The results hereby presented demonstrate that the presented EFPI/FBG technology is capable of
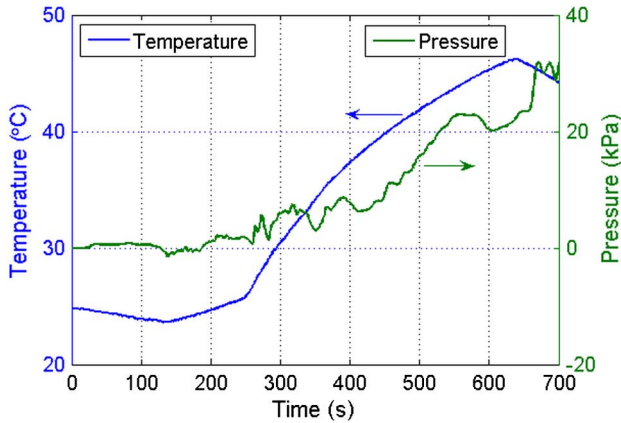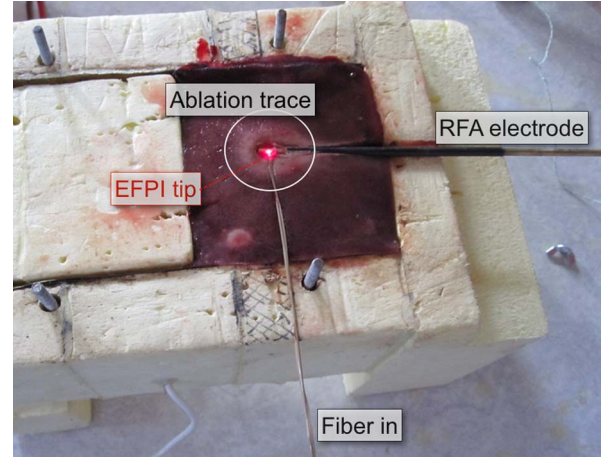

Fig. 12. Setup for third *ex vivo* RFA experiment: porcine liver has been inserted in a small chamber to facilitate positioning. Electrode and optical fiber probe are inserted perpendicularly, with a 0.5 cm misalignment between the two tips, only a few millimeters below the liver tissue. The picture, taken after the ablation, shows elliptical shape traces with the thermal lesion (light colored tissue). The optical fiber tip is illuminated with a red laser, and is located in close proximity of the center of the ablation lesion; the illumination shows the 0.5 cm misalignment between the electrode tip and the fiber output.

monitoring the RFA process, unlike traditional MEMS sensors and standard fiber-optic sensors. In order to improve the pressure readout, it is necessary to introduce a high-reflectivity layer in order to neutralize the effect of the liver medium on the EFPI spectrum. However, the results presented are a good indicator of the effectiveness of the sensing technology, and pave the road for online RFA monitoring *in vivo*. In particular, the peak values (164°C, 162 kPa) obtained in the second *ex vivo* experiment demonstrate that during RFA it is possible to reach temperature and pressure values higher than previous measurement, due to the small active areas of EFPI and FBG. Such result will be further expanded by providing a dense monitoring of the RFA process, with a plurality of EFPI/FBG probes multiplexed in a single interrogator.

6. Conclusion

In this paper, we presented a combined EFPI/FBG probe, based on an all-glass biocompatible design, which performs pressure and temperature estimation with cross compensation. The EFPI has a sensitivity of 1.60 nm/kPa, and an extremely low thermal sensitivity (0.0519 nm/°C), while the FBG shows temperature sensitivity of 10.70 pm/°C. To the best of our knowledge, the EFPI thermal sensitivity is the lowest ever achieved for an EFPI sensor, and is over 30 times smaller than standard all-glass structures. A measurement campaign has been carried out, first heating with a uniform RF EM field a test chamber with saline solution and liver tissue, and second applying RFA on *ex vivo* porcine liver tissue. Experimental measurements showed that both temperature and pressure have an extremely steep

Fig. 11. Third RFA experiment: temperature and pressure traces.

gradient: temperature peaks of 31°C, 46°C, and 164°C, and pressure peaks of 6, 33, and 162 kPa have been obtained by positioning the probe, respectively, 8, 5, and 1 mm far from the electrode tip. These results, which partially overcome the previous RFA literature, set the basis for a dense pressure/temperature monitoring during thermal ablation.

References

1. B. J. Wood, J. R. Ramkaransingh, M. S. Tito Fojo, M. M. Walther, and S. K. Libutti, "Percutaneous tumor ablation with radiofrequency," Cancer **94**, 443–451 (2002).
2. L. Solbiati, T. Livraghi, S. Nahum Goldberg, T. Ierace, F. Meloni, M. Dellanoce, L. Cova, E. F. Halpern, and G. S. Gazelle, "Percutaneous radio-frequency ablation of hepatic metastases from colorectal cancer: long-term results in 117 patients," Radiology **221**, 159–166 (2001).
3. A. Orlando, G. Leandro, M. Olivo, A. Andriulli, and M. Cottone, "Radiofrequency thermal ablation vs percutaneous ethanol injection for small hepatocellular carcinoma in cirrhosis: meta-analysis of randomized controlled trials," Am. J. Gastroenterol. **104**, 514–524 (2009).
4. S. N. Goldberg, G. S. Gazelle, and P. R. Mueller, "Thermal ablation therapy for focal malignancy: a unified approach to underlying principles, techniques, and diagnostic imaging guidance," Am. J. Roentgen. **174**, 323–331 (2000).
5. P. L. Pereira, "Actual role of radiofreqency ablation of liver metastases," European Radiol. **7**, 291–299 (2007).
6. M. J. Dodd, "Radiofrequency ablation of the liver: current status," Am. J. Roentgen. **176**, 3–16 (2001).
7. S. Padma, J. B. Martinie, and D. A. Iannitti, "Liver tumor ablation: percutaneous and open approaches," J. Surg. Oncol. **100**, 619–634 (2009).
8. S. Curley, "Radiofrequency ablation of malignant liver tumors," Ann. Surg. Oncol. **1**, 338–347 (2003).
9. M. Sato, Y. Watanabe, S. Ueda, S. Iseki, Y. Abe, N. Sato, S. Kimura, K. Okubo, and M. Onji, "Microwave coagulation therapy for hepatocellular carcinoma," Gastroenterology **110**, 1507–1514 (1996).
10. T. Shibata, Y. Iimuro, Y. Yamamoto, Y. Maetani, F. Ametani, K. Itoh, and J. Konishi, "Small hepatocellular carcinoma: comparison of radio-frequency ablation and percutaneous microwave coagulation therapy," Radiology **223**, 331–337 (2002).
11. F. Ahmad, G. Gravante, N. Bhardwai, A. Strickland, R. Basit, and R. Sorge, "Large volume hepatic microwave ablation elicits fewer pulmonary changes than radiofrequency or cryotherapy," J. Gastrointest. Surg. **14**, 1963–1968 (2010).
12. C. M. Pacella, G. Bizzarri, F. Magnolfi, P. Cecconi, B. Caspani, V. Anelli, A. Bianchini, D. Valle, S. Pacella, G. Manenti, and Z. Rossi, "Laser thermal ablation in the treatment of small hepatocellular carcinoma: results in 74 patients," Radiology **221**, 712–720 (2001).
13. M. Ahmed, C. L. Brace, F. T. Lee, and S. N. Goldberg, "Principles of and advances in percutaneous ablation," Radiology **258**, 351–369 (2011).
14. M. Trujillo, J. Alba, and E. Berjano, "Relationship between roll-off occurrence and spatial distribution of dehydrated tissue during RF ablation with cooled electrodes," Int. J. Hyperthermia **28**, 62–68 (2012).
15. K. Kotoh, M. Enjoji, E. Arimura, S. Morizono, M. Kohjima, H. Sakai, and M. Nakamuta, "Scattered and rapid intrahepatic recurrences after radio frequency ablation for hepatocellular carcinoma," World J. Gastroenterol. **11**, 6828–6832 (2005).
16. K. Kotoh, M. Nakamuta, S. Morizono, M. Kohjima, E. Arimura, M. Fukushima, M. Enjoji, H. Sakai, and H. Nawata, "A multi-step, incremental expansion method for radio frequency ablation: optimization of the procedure to prevent increases in intra-tumor pressure and to reduce the ablation time," Liver Int. **25**, 542–547 (2005).
17. M. Nakamuta, M. Kohjima, S. Morizono, T. Yoshimoto, Y. Miyagi, H. Sakai, M. Enjoji, and K. Kotoh, "Comparison of tissue pressure and ablation time between the LeVeen and cool-tip needle methods," Comp. Hepatol. **5**, 10 (2006).
18. E. Udd and W. B. Spillman, *Fiber Optic Sensors: An Introduction for Engineers and Scientists* (Wiley Interscience, 1991).
19. Y.-J. Rao, "Recent progress in fiber-optic extrinsic Fabry–Perot interferometric sensors," Opt. Fiber Technol. **12**, 227–237 (2006).
20. P. Roriz, O. Frazao, A. B. Lobo-Ribeiro, J. L. Santos, and J. A. Simoes, "Review of fiber-optic pressure sensors for biomedical and biomechanical applications," J. Biomed. Opt. **18**, 050903 (2013).
21. K. K. Chin, Y. Sun, G. Feng, G. E. Georgiou, K. Guo, E. Niver, H. Roman, and K. Noe, "Fabry–Perot diaphragm fiber-optic sensor," Appl. Opt. **46**, 7614–7619 (2007).
22. F. Xu, D. Ren, X. Shi, C. Li, W. Lu, L. Lu, L. Lu, and B. Yu, "High-sensitivity Fabry–Perot interferometric pressure sensor based on a nanothick silver diaphragm," Opt. Lett. **37**, 133–135 (2012).
23. L. H. Chen, C. C. Chan, W. Yuan, S. K. Goh, and J. Sun, "High performance chitosan diaphragm-based fiber-optic acoustic sensor," Sens. Actuators A **163**, 42–47 (2010).
24. P. Polygerinos, D. Zbyszewski, T. Schaeffter, R. Razavi, L. D. Seneviratne, and K. Althoefer, "MRI-compatible fiber-optic force sensors for catheterization procedures," IEEE Sens. J. **10**, 1598–1608 (2010).
25. M. Zhou, C. Yang, Z. Liu, J. P. Cysyk, and S. Zheng, "An implantable Fabry–Perot pressure sensor fabricated on left ventricular assist device for heart failure," Biomed. Microdevices **14**, 235–245 (2012).
26. K. Bremer, E. Lewis, B. Moss, G. Leen, S. Lochmann, and I. Mueller, "Conception and preliminary evaluation of an optical fibre sensor for simultaneous measurement of pressure and temperature," J. Phys. Conf. Ser. **178**, 012016 (2009).
27. K. Bremer, E. Lewis, G. Leen, B. S. Lochmann, and I. A. R. Mueller, "Feedback stabilized interrogation technique for EFPI/FBG hybrid fiber-optic pressure and temperature sensors," IEEE Sens. J. **12**, 133–138 (2012).
28. H. Bae and M. Yu, "Miniature Fabry–Perot pressure sensor created by using UV-molding process with an optical fiber based mold," Opt. Express **20**, 14573–14583 (2012). Opsens
29. OPP-M, http://www.opsens.com/en/industries/products/pressure/opp-m/.
30. Y. J. Rao, "In-fibre Bragg grating sensors," Meas. Sci. Technol. **8**, 355–375 (1997).
31. A. Othonos and K. Kalli, "Properties of fiber Bragg gratings," in *Fiber Bragg Gratings: Fundamentals and Applications in Telecommunications and Sensing* (Artech House, 1999), pp. 95–147.
32. K. O. Hill, B. Malo, F. Bilodeau, D. C. Johnson, and J. Albert, "Bragg gratings fabricated in monomode photosensitive optical fiber by UV exposure through a phase mask," Appl. Phys. Lett. **62**, 1035–1037 (1993).
33. S. Poeggel, D. Tosi, G. Leen, and E. Lewis, "Diaphragm etching in extrinsic Fabry–Perot interferometric fiber-optic pressure sensors," in Conference on Lasers and Electro-Optics (CLEO) Europe, Munich, Germany (2013).
34. Y. Jiang and W. Ding, "Recent developments in fiber optic spectral white-light interferometry," Photonic Sens. **1**, 62–71 (2011).
35. D. Tosi, M. Olivero, G. Perrone, and A. Vallan, "Weigh-in-motion through fibre Bragg grating optical sensors," Electron. Lett. **46**, 1223–1225 (2010).